

# High-spatial-resolution near-field photoluminescence and imaging of whispering-gallery modes in semiconductor microdisks with embedded quantum dots

A. M. Mintairov,<sup>1</sup> Y. Chu,<sup>1</sup> Y. He,<sup>1</sup> S. Blokhin,<sup>2</sup> A. Nadochy,<sup>2</sup> M. Maximov,<sup>2</sup> V. Tokranov,<sup>3</sup> S. Oktyabrsky,<sup>3</sup> and J. L. Merz<sup>1</sup>

<sup>1</sup>University of Notre Dame, Notre Dame, Indiana 46556, USA

<sup>2</sup>Ioffe Physico-Technical Institute, St. Petersburg, Russia

<sup>3</sup>Institute for Materials, SUNY Albany, Albany, New York 12203, USA

(Received 15 April 2008; published 23 May 2008)

Near-field photoluminescence (NPL) spectroscopy with a spatial resolution below the light diffraction limit was used to study the optical fields of whispering-gallery modes (WGMs) in GaAs and AlGaAs microdisks (radii  $R=1-3\ \mu\text{m}$  and quality factors  $Q\sim 5\times 10^3$ ) containing InAs quantum dots (QDs). WGMs with azimuthal mode numbers  $m=10-36$  and radial mode numbers  $l=1-3$ , together with low- $Q$  Fabry-Pérot modes and other non-WGMs, have been resolved in NPL spectra in the range of  $1.1-1.3\ \mu\text{m}$ . We found that spectrally resolved NPL intensity images of the WGMs reveal  $m$  azimuthal maxima around the disk circumference, which correspond to the period of the field amplitude. Using finite-difference-time-domain (FDTD) calculations, we show that the amplitude imaging arises from the interference between the WGMs and a background field formed by low- $Q$  modes. We show further that such interference reflects the inhomogeneity of the radiation decay of the QD ensemble in the MD. We demonstrate a direct measurement of WGM quantum numbers in microdisks by using NPL imaging, which shows good agreement with FDTD calculations.

DOI: [10.1103/PhysRevB.77.195322](https://doi.org/10.1103/PhysRevB.77.195322)

PACS number(s): 42.55.Sa, 42.50.Pq, 78.55.Cr, 78.67.Hc

## I. INTRODUCTION

Semiconductor microdisks (MDs) represent very efficient optical resonators for light propagating along the disk circumference due to total internal reflection, forming the so-called whispering-gallery modes (WGMs).<sup>1,2</sup> Quality factors ( $Q$ ) as high as  $10^6$  can be achieved for fundamental WGMs in such disks.<sup>3</sup> Through a self-organized epitaxial growth on the initial planar structures, an ensemble of quantum dots having atomlike radiative excitonic transitions can be naturally embedded in MDs.<sup>4</sup> Such a high- $Q$  nanophotonic system exhibits extremely low lasing thresholds<sup>5</sup> and makes possible the observation of the vacuum Rabi splitting (strong photon-exciton coupling in cavity-quantum electrodynamics<sup>6</sup>) for individual quantum dots (QDs) in the low temperature emission spectra.<sup>7</sup> By using different semiconductor materials, it is possible to observe emission energies throughout the spectral range from the violet to the near-infrared ( $0.4-1.6\ \mu\text{m}$ ).<sup>8-10</sup> The emission spectra of the QD ensemble can be used to map optical fields associated with WGMs in MDs by using the near-field scanning optical microscopy (NSOM) technique, which is similar to the optical field mapping of photonic crystal cavities.<sup>11,12</sup> Such near-field mapping, having a spatial resolution below the light diffraction limit, allows direct measurements of the quantum numbers of WGMs<sup>13</sup> and is important for nanophotonic applications, including low-threshold lasers, single photon sources,<sup>14</sup> and quantum information processing.<sup>15</sup> The development of the NSOM technique in terms of probing MD optical fields provides additional possibilities for solid-state cavity-quantum electrodynamics experiments, such as the control of spatial and spectral matching of the cavity mode with the QD exciton through topographical information<sup>16</sup> and nanoindentation.<sup>17</sup> At the present time, there are only a

few reports of near-field photoluminescence imaging of semiconductor MDs, and in these reports, QDs were not used as the active material<sup>18,19</sup> and the mode structure was not determined. The WGM field structure with a spatial resolution below the diffraction limit was, however, resolved for a passive ring cavity at  $\lambda=633\ \text{nm}$ .<sup>20</sup>

In the present paper, we use near-field photoluminescence (NPL) spectroscopy with a spatial resolution below the light diffraction limit to study optical fields of whispering-gallery modes (WGMs) in GaAs and AlGaAs microdisks (radii  $R=1-3\ \mu\text{m}$  and quality factors  $Q\sim 5\times 10^3$ ) containing InAs QDs emitting in the range of  $1.1-1.3\ \mu\text{m}$ . The WGMs having azimuthal numbers  $m=10-36$  and radial numbers  $l=1-3$ , together with low- $Q$  Fabry-Pérot modes (FPMs) and other non-WGMs, have been observed in the NPL spectra. We found that spectrally resolved NPL images of WGMs reveal field amplitude periods, i.e.,  $m$  azimuthal maxima. Using finite-difference-time-domain (FDTD) calculations, we show that the amplitude imaging arises from the interference between the WGMs and a background field formed by low- $Q$  modes. We show that such interference reflects a strong inhomogeneity of the radiation decay of the QD ensemble in the MDs. We demonstrate a direct measurement of WGM quantum numbers by using NPL imaging, which shows a good agreement with FDTD calculations.

## II. EXPERIMENTAL DETAILS

Microdisks studied in this work were prepared from two 230–270 nm thick GaAs and AlGaAs waveguide structures with embedded self-organized InAs quantum dots formed in the Stranski-Krastanov growth mode by molecular beam epitaxy. The waveguide structures were grown on the top of

an AlAs layer having a thickness of 500 nm, which was grown on GaAs substrate. The density of QDs [ $(2-5) \times 10^{10} \text{ cm}^{-2}$ ] was determined by transmission electron microscopy (TEM). The first, the GaAs structure, consists of a GaAs waveguide with a single QD layer emitting at  $\lambda \sim 1.3 \mu\text{m}$  and was used for fabrication of a MD having  $R = 3 \mu\text{m}$  by using optical lithography, reactive ion etching, and wet thermal oxidation of the AlAs layer, as described in Refs. 21 and 22. The second, the AlGaAs structure, consists of an AlAs/GaAs short-period superlattice waveguide, with a single QD layer emitting at  $\lambda \sim 1.2 \mu\text{m}$ , as described in Ref. 23. For this structure, the waveguide was wafer bonded to Si substrate by using a silicate glass precursor (Filmtronics, Inc.) solution. Then, the GaAs substrate and the AlAs layer were removed by mechanical polishing and chemical etching. Finally, the MDs having  $R = 1$  and  $2 \mu\text{m}$  were prepared by using electron beam lithography and reactive ion etching. We should point out that our GaAs and AlGaAs MDs have asymmetric-waveguide design. Such a design provides a higher thermal conductivity, a lower optical loss, and an enhanced mechanical stability compared to those of traditional mushroomlike microdisks. The enhanced mechanical stability is important for nanoindentation experiments. Scanning electron microscope (SEM) images of the MDs reveal radius deviations of 20 nm.

Optical measurements were done at room temperature. Microphotoluminescence and near-field photoluminescence (NPL) spectra were excited at a power of 10–100  $\mu\text{W}$  by using the 488 nm line from an Ar ion laser and measured by using a 270 mm focal length spectrometer and liquid-nitrogen-cooled multichannel InGaAs- or single-channel Ge detector. The spectral resolution was 0.3 nm. NPL spectra and images were measured by using a NANONICS Multi-View 1000 head and scanning probe microscopy (SPM) controller. Uncoated fiber probes (tips) were used that had an apex of 300 nm and a taper angle of  $40^\circ$ – $50^\circ$  (Ref. 17); these provided a spatial resolution as high as  $\sim 300$  nm (Refs. 24 and 25) in the near-infrared spectral range ( $\lambda \sim 1.1$ – $1.3 \mu\text{m}$ ). NPL spectra were excited and collected through the same fiber probe. Due to the absence of a metal coating to confine the light in the taper of the tip, such probes provide a far-field excitation area of a few micrometers in size but detection of the evanescent field by the probe. Lock-in-amplifier detection was used to obtain  $128 \times 128$  pixel NPL images in a spectral window of 0.6–1.2 nm with a 30 ms accumulation time at each pixel.

### III. MICROPHOTOLUMINESCENCE SPECTRA

Figures 1(a) and 1(b) show the microphotoluminescence ( $\mu$ -PL) spectra and SEM images of  $R = 3 \mu\text{m}$  [Fig. 1(a)] and  $R = 2$  and  $1 \mu\text{m}$  [Fig. 1(b)] cavities together with the spectra of the initial planar GaAs and AlGaAs wafers and plan-view TEM images of the QDs. The ensemble emission of unprocessed wafers consists of two spectral bands related to the ground and excited states of InAs QDs (note the different ground state emission wavelengths of the GaAs and AlGaAs structures). The bands have a width ( $\gamma_{\text{ensemble}}$ ) of 60 (40) nm and a separation 90 (110) nm for the GaAs (AlGaAs) struc-

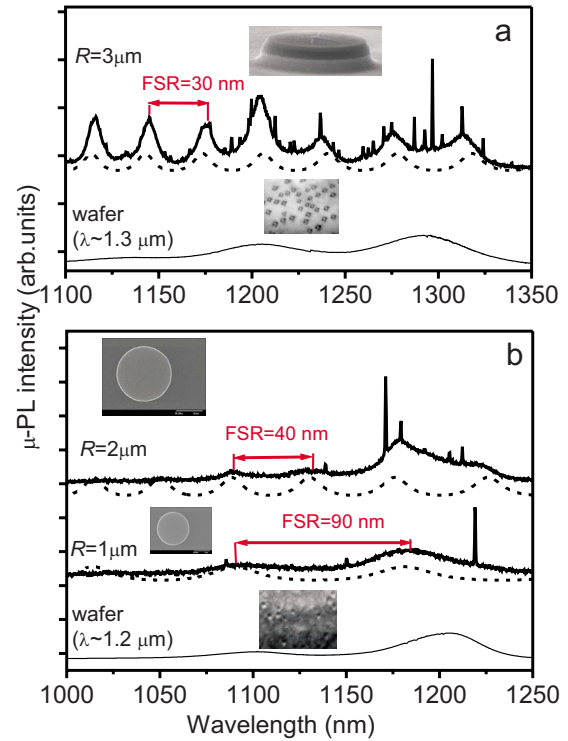


FIG. 1. (Color online)  $\mu$ -PL spectra (solid curves) of InAs QDs embedded in GaAs ( $\lambda \sim 1.3 \mu\text{m}$ ) and AlGaAs ( $\lambda \sim 1.2 \mu\text{m}$ ) MDs having  $R$ : (a)  $3 \mu\text{m}$  and (b)  $1$  and  $2 \mu\text{m}$  spectra (thin solid curves) are  $\mu$ -PL spectra of unprocessed wafers. The dotted curves are Fabry-Pérot etalon transmission for thickness of  $2R$ . The insets are the SEM images of MDs (upper) and  $0.24 \times 0.32 \mu\text{m}^2$  TEM images of InAs QDs (lower).

tures. The MD spectra reveal a characteristic periodic structure consisting of few sharp lines (from one for  $R = 1$  to six for  $R = 3 \mu\text{m}$ ) superimposed on a broad band, which are repeated with free spectral range (FSR) periods of  $\sim 30$ , 40, and 90 nm for  $R = 3$ , 2, and  $1 \mu\text{m}$ , respectively. The sharp lines are related to WGMs, while the broad bands are related to lateral FPMs. The FPMs originate from light bouncing along the cavity diameter; the reflection function of a planar Fabry-Pérot etalon having a thickness of  $2R$  reproduces well the positions and period of these bands, as seen in the  $\mu$ -PL spectra of each MD [see Figs. 1(a) and 1(b)]. In the high spatial resolution spectra discussed below, we have also observed another type of modes, which we called confined modes (CMs).<sup>26</sup> Such modes are equivalent to the HE  $(\text{EH})_{m,l}$  modes of cylindrical waveguides,<sup>27</sup> which are confined by the finite thickness of the disk ( $\sim \lambda/2n$ , where  $n$  is the refractive index). Such modes are localized at the disk center and dominate in micropillar cavities.<sup>28</sup> The  $Q$  factors were estimated to be  $\sim 4 \times 10^3$  for WGMs and  $\sim 50$  for FPMs. From these  $Q$  factors, one calculates the decay of the cavity modes to be 2 and 0.05 ps, respectively, which are much shorter than the radiation decay of InAs QDs,  $\tau_r = 100$ – $1000$  ps,<sup>29,30</sup> and corresponds to a weak-coupling regime.<sup>6</sup> Using the width of the single emission lines  $\gamma_{\text{single}} \sim 10$  nm,<sup>31,32</sup> determining a portion of the QD ensemble resonant to WGM ( $\gamma_{\text{single}}/\gamma_{\text{ensemble}}$ ), the number of resonant QDs can be estimated to be  $10^2$ – $10^3$  for  $R = 1$ – $3 \mu\text{m}$  MDs.

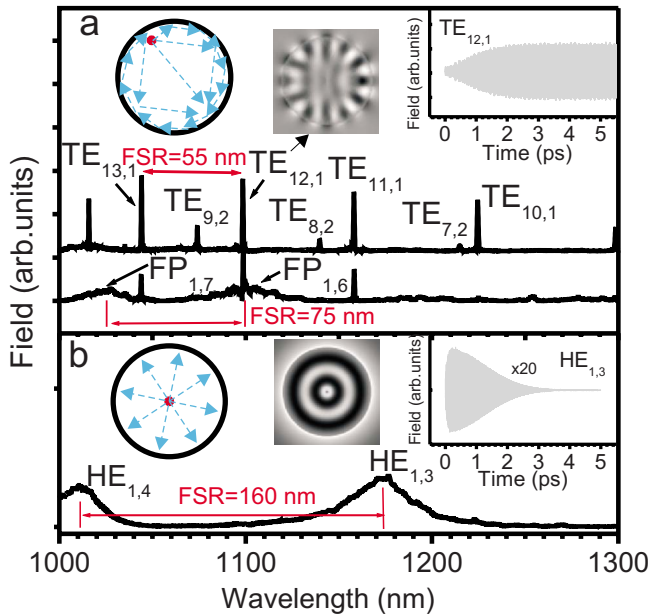


FIG. 2. (Color online) Near-field spectra of  $R=1 \mu\text{m}$  MD calculated by FDTD for (a) edge and (b) center TE excitations ( $\tau_1=20$  fs). The center insets are the calculated patterns of the radial electric field at  $t=0.4$  ps. The right insets are the calculated time decays of the (a)  $\text{TE}_{12,1}$  and (b)  $\text{HE}_{1,3}$  modes ( $\tau_2=2$  ps). The left insets show the source position (dot) and light passes (arrows) in the MD. Spectra and decays were calculated at field maxima nearest to the excitation source.

#### IV. FINITE-DIFFERENCE-TIME-DOMAIN CALCULATIONS AND NEAR-FIELD SCANNING OPTICAL MICROSCOPY IMAGING

The calculations of mode spectra, field and/or intensity distributions, and  $Q$  factors were done by using the FDTD commercial software by Lumerical, Inc. The FDTD method numerically solves the time-dependent Maxwell equations for the electromagnetic field excited in the cavity by a point dipole.<sup>33–35</sup> It provides the oscillating components of the electric and magnetic fields in the nodes of a three-dimensional spatial grid. A Fourier transformation of these fields generates mode spectra. We used a spatial grid with cell  $\Delta x \Delta y \Delta z = 8 \times 8 \times 4 \text{ nm}^3$  and time steps  $\Delta t = 0.53926$  fs. An excitation pulse with decay time  $\tau_1 = 10\text{--}20$  fs (broad band excitation) was used to calculate the mode spectra. Decay times  $\tau_2 = 1\text{--}2$  ps (narrow band excitation) at resonance with specific modes were used to generate field patterns for these modes. The field patterns were used for the determination of the azimuthal ( $m$ ) and radial ( $l$ ) mode numbers<sup>2</sup> and were calculated 4 nm above the disk. To account for the effects of the cavity wall imperfections, we used disk shapes taken from the SEM images. The effect of the probe was analyzed by placing a  $1 \mu\text{m}$  long  $\text{SiO}_2$  taper segment 8 nm above the disk. The  $Q$  factors were calculated from the decay of the field intensity. We did not account in our calculation for the dispersion of the material's refractive index.

Figures 2(a) and 2(b) show the results of the FDTD analysis of the TE modes for an ideal MD having  $R=1 \mu\text{m}$ . Here,

a vertically oriented electric dipole excitation ( $\tau_2=2$  ps) was placed either 140 nm from the edge [Fig. 2(a)] or at the center [Fig. 2(b)], as shown by the dots in the left insets. The spectra and the field decays presented in Fig. 2(b) were calculated at positions of field maxima, which are determined from the field patterns. From the cartoons in the left insets in Figs. 2(a) and 2(b), which show light propagation passes, it is evident that the WGMs and FPMs, forming waves traveling along the disk circumference and the chords, respectively, are excited by the edge source, and that the CMs, forming radial waves, are excited by the central source. From the selected mode spectra presented, one can see that at the edge excitation, the sharp lines related to  $\text{TE}_{m,1}$  ( $m=10\text{--}12$ ) and  $\text{TE}_{m,2}$  ( $m=7\text{--}9$ ) WGMs and broad  $\text{FP}_{1,l}$  ( $l=4\text{--}7$ ) FPM bands appear in the range of 1000–1300 nm [see Fig. 2(a)]. For the center excitation [Fig. 2(b)], no sharp WGMs appear; only broad CM bands  $\text{HE}_{1,l}$  ( $l=3$  and 4) are seen in this spectral range. The CMs have FSR of 160 nm, which is more than twice that of the FPMs, which enables them to be distinguished in the spectra. Envelopes of the time evolution of the  $\text{TE}_{12,1}$  and  $\text{HE}_{1,5}$  mode fields are presented in the right insets of Figs. 2(a) and 2(b), respectively. For the  $\text{TE}_{12,1}$  WGM, the field increases during  $\tau_2$  (1–2 ps) and then decreases with decay time  $\tau_{\text{WGM}}=20$  ps ( $Q=10^4$ ). For CMs ( $\tau_{\text{CM}}=0.02$  ps), the field follows the decay of the excitation. Inspection of the field patterns shows that the field amplitudes of FPMs and CMs are nearly one-half of WGMs at  $t \sim \tau_2/5$ , and then, they become an order of magnitude smaller at  $t \sim \tau_2$ . The patterns at  $\tau_2/5$  are shown in the center inset of Figs. 2(a) and 2(b). At edge excitation, the features of both WGMs and FPMs are revealed in Fig. 2(a). Here,  $m$  field maxima and  $m$  field minima aligned along the circumference are seen for the  $\text{TE}_{12,1}$  mode. They are elongated along the radial direction and have a radial size of  $\sim 400$  nm, which is close to  $\lambda/n$ . The azimuthal size of the maxima is  $\sim 200$  nm, which is  $\sim \pi R/m$ . The field related to the FPM reveals modulations along the horizontal ( $x$ ) axis over the entire disk with period  $\sim \lambda/n \sim 2R/l$ . The field pattern for the  $\text{HE}_{1,3}$  CM in Fig. 2(b) consists of concentric rings with spacing  $\sim \lambda/n \sim R/l$ .

The calculations for other disk sizes have shown that for  $R=2 \mu\text{m}$ , the  $\text{TE}_{1,m}$  ( $m=24\text{--}28$ ),  $\text{TE}_{2,m}$  ( $m=20\text{--}24$ ),  $\text{TM}_{1,m}$  ( $m=21\text{--}25$ ), and  $\text{TM}_{2,m}$  ( $m=17\text{--}21$ ) WGMs are dominant in the AlGaAs structure emission spectral range of 1050–1250 nm and that for  $R=3 \mu\text{m}$   $\text{TE}_{1,m}$  ( $m=34\text{--}42$ ),  $\text{TE}_{2,m}$  ( $m=31\text{--}39$ ),  $\text{TE}_{3,m}$  ( $m=26\text{--}32$ ),  $\text{TM}_{1,m}$  ( $m=26\text{--}32$ ), and  $\text{TM}_{2,m}$  ( $m=23\text{--}31$ ) WGMs are dominant in the GaAs structure emission spectral range of 1150–1350 nm. Inspection of the field patterns has shown that the maxima of TM modes have smaller radial size than TE modes. For example, the size of  $\text{TE}_{1,24}$  and  $\text{TM}_{1,21}$  mode maxima ( $R=2 \mu\text{m}$ ) are  $600 \times 200$  and  $400 \times 300 \text{ nm}^2$  and the size of  $\text{TE}_{1,37}$  and  $\text{TM}_{1,27}$  mode maxima ( $R=3 \mu\text{m}$ ) are  $700 \times 250$  and  $600 \times 300 \text{ nm}^2$ .

We found that the fiber has only a minor effect on the field patterns: its loading of the cavity produces mode shifts of less than 1 nm and enhancement of the TM-mode intensities and reduction of the  $Q$  factor by less than 30%. The calculated unloaded  $Q$  factors for the lowest radial order WGM  $\text{TE}_{m,1}$  are  $Q \sim 10^4$ ,  $10^6$ , and  $>10^8$  for  $m \sim 10$ , 25, and 35 and

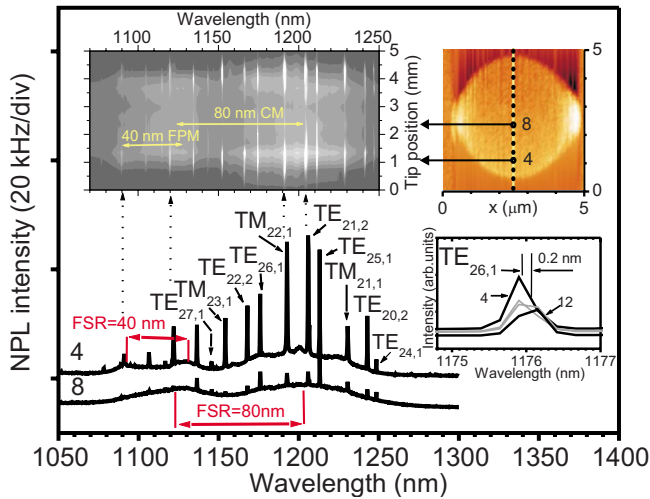


FIG. 3. (Color online) Near-field spectra of the  $R=2 \mu\text{m}$  MD taken at positions 4 ( $x/y=2.5/1.2 \mu\text{m}$ ) and 8 ( $x/y=2.5/2.4 \mu\text{m}$ ), which are marked by large dots in the disk topographic image in the upper right inset. The upper left inset shows a three-dimensional contour plot of spatially resolved NPL spectra taken by using a linear scan along the disk diameter (see topography for tip positions). The lower right inset shows the  $\text{TE}_{26,1}$  mode line in the NPL spectra at four tip positions.

$R=1, 2,$  and  $3 \mu\text{m}$ , respectively. However, we found that when the measured wall imperfections were taken into account, the  $Q$  factors are reduced to  $(\sim 2-5) \times 10^3$  (in agreement with experiment) and the wavelength is shifted up to 20 nm. The latter was used as an uncertainty value for the mode positions calculated for an ideal disk. The calculations also show that the azimuthal position of the field maxima depends on the azimuthal position of the excitation source, which indicates that there is no WGM localization on wall roughness.

Since our probes work in a collection-mode regime (i.e., far-field excitation and near-field collection), the specific WGM detected in the NSOM experiment is excited by the emission of all resonant QDs in the MD; the resulting field is therefore a superposition of the WGM with the FPMs and the CMs, which is excited by differently located QDs. The time-averaged field coupled to a near-field probe and detected at a resonance wavelength will depend on the radiation decay of QDs at different locations, as shown in Figs. 2(a) and 2(b). For a QD ensemble, the reabsorption of a WGM can also affect the radiation time. The simplest assumptions will be that the radiative lifetime  $\tau_r$  will be independent of QD position (homogeneous decay) and that there will be no reabsorption of a WGM. For our cavities, working in a weak-coupling regime, this corresponds to a dominance of the WGM mode in the time-averaged field (see below). In this case, the NPL intensity images will resolve the WGM mode intensity structure.

## V. NEAR-FIELD SCANNING OPTICAL MICROSCOPY SPECTRA AND IMAGES

Figure 3 presents the results of the analysis of the experimental NPL spectra for  $R=2 \mu\text{m}$  taken by using a linear

scan along the disk diameter. The 16 points (scan step of 330 nm) at which spectra were taken are marked in the  $5 \times 5 \mu\text{m}^2$  topographic image in the upper right inset. Figure 3 shows two representative NPL spectra in the range of 1050–1300 nm taken near the center (point 8) and near the edge (point 4) (see upper right inset). The inset above the spectra shows a distribution (image) of the spectral intensity along the scan line. The sharp lines result from WGMs and the broad bands result from FPMs and CMs, as can be clearly observed in the spectra and image in Fig. 3. In agreement with the FDTD analysis, the WGMs and FPMs appeared in the spectra detected near the disk edge (position 4), while the CMs dominate when the spectra are detected near the center (position 8). The CMs were distinguished by their FSR value (80 nm for  $R=2 \mu\text{m}$ ), which is nearly twice that of the FPMs (and half that of the CM FSR for the  $1 \mu\text{m}$  disk, see Fig. 2). The CMs are very broad and have a width of  $\sim 60 \text{ nm}$ , which is nearly three times larger than the width of FPMs. Comparing the  $\mu\text{-PL}$  [Fig. 1(b)] and NPL spectra (Fig. 3) of this MD, one can see a strong enhancement of TM modes in the NPL spectrum compared to the  $\mu\text{-PL}$  spectrum (see  $\text{TM}_{22,1}$  mode at  $\sim 1190 \text{ nm}$ ), which is in agreement with FDTD calculations. We also observed the 0.2 nm variation of the WGM position (see the lower right inset for the  $\text{TE}_{26,1}$  mode) along the scan line, which is also reproduced in the calculations.

Figures 4(a)–4(c) present the NPL images of 15 selected WGMs and spectra showing mode positions for  $R=1, 2,$  and  $3 \mu\text{m}$ . Figures 4(a)–4(c) include mode assignments obtained from image analysis and the FDTD calculations discussed below. The topographic images of the cavities are also presented in Figs. 4(a)–4(c). The inset of Fig. 4(c) shows a radial cut (profile) of the  $\text{TE}_{11,1}$  mode image along a line running from 5 o'clock to 11 o'clock in the mode image. In Figs. 4(d) and 4(e), we show enlarged images of  $\text{TE}_{35,1}$ ,  $\text{TE}_{32,2}$ , and  $\text{TE}_{24,3}$  modes of  $R=3 \mu\text{m}$  (scale  $7 \times 7 \mu\text{m}^2$ ) and  $\text{TE}_{24,1}$ ,  $\text{TE}_{21,2}$ , and  $\text{TM}_{21,1}$  modes of  $R=2 \mu\text{m}$  (scale  $5 \times 5 \mu\text{m}^2$ ), respectively. An enlarged scale ( $1 \times 1 \mu\text{m}^2$ ) image of “excerpts” of modes  $\text{TM}_{22,1}$ ,  $\text{TE}_{25,1}$ ,  $\text{TE}_{35,1}$ , and  $\text{TE}_{10,1}$  modes is shown in Fig. 4(f). Figure 4(g) presents the results of the simulation of  $\text{TE}_{12,1}$  intensity (insets 1, 2, and 3) and NPL images (insets 4 and 6) for different simulation conditions, as described in the caption, and their comparison to experiment (inset 5).

One can see from Figs. 4(a)–4(f) that the measured NPL images of WGM spectral lines clearly show resolved bright maxima azimuthally aligned along the disk circumference. Most of the maxima can be clearly resolved despite some topographical artifacts (distortions at the vertical edges of the disk and acoustic noise of the scanner) and a saturation of the lock-in-amplifier in some images [dark spots in images of  $\text{TE}_{32,2}$  and  $\text{TE}_{24,3}$  modes in Fig. 4(d)]. A single set of azimuthal maxima is seen for the lowest radial order ( $l=1$ ) modes  $\text{TE}_{35,1}$ ,  $\text{TM}_{21,1}$ , and  $\text{TE}_{24,1}$  in Figs. 4(d) and 4(e). Additional sets of maxima (one for  $l=2$  and two for  $l=3$ ), which are shifted  $\sim 500 \text{ nm}$  toward the disk center, are seen for higher radial orders ( $\text{TE}_{32,2}$ ,  $\text{TE}_{21,2}$ , and  $\text{TE}_{24,3}$  modes). The TE- and TM-type modes have different average sizes of the maxima, which are  $\sim 300 \times 500 \text{ nm}^2$  for TE modes and  $\sim 400 \times 400 \text{ nm}^2$  for TM modes, respectively, for  $l=1$  [see

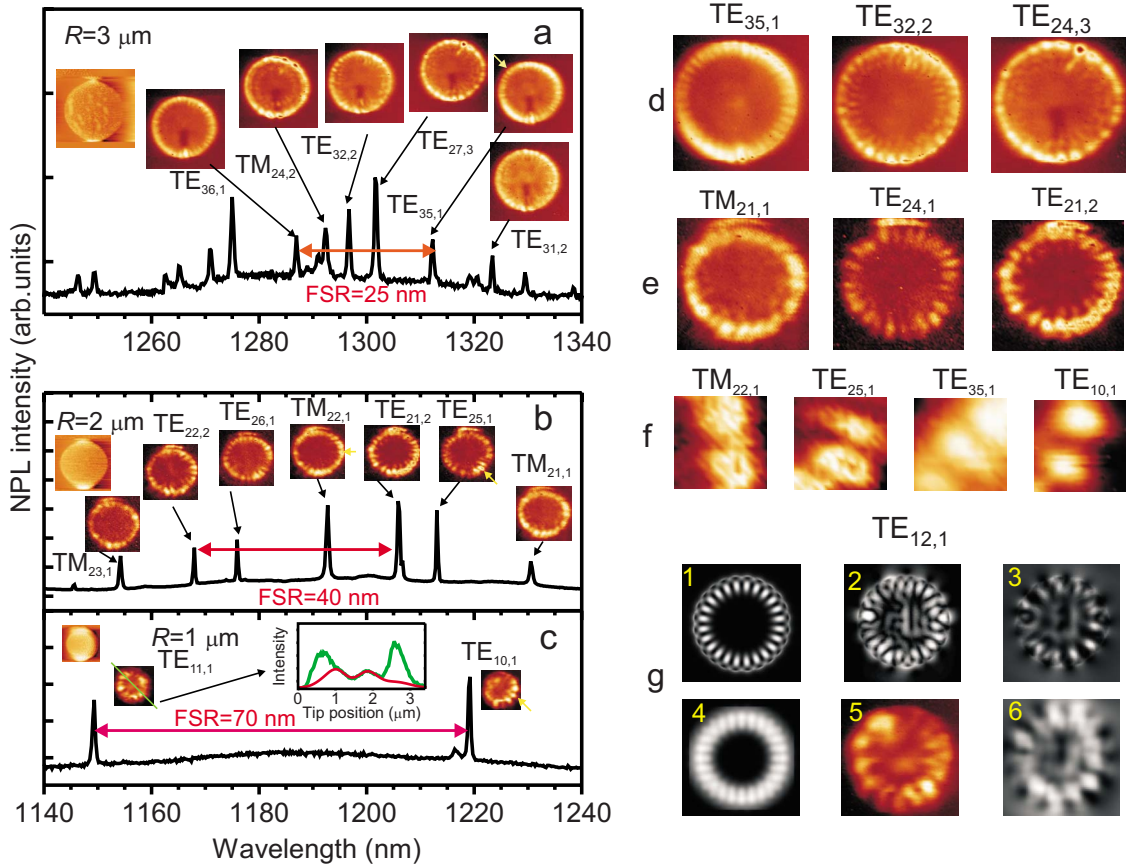


FIG. 4. (Color online) NPL spectra and images of 15 WGM spectral lines of MDs having  $R(\mu\text{m})$ : (a) 3, (b) 2, and (c) 1, together with [(d)–(f)] the enlarged images of nine selected WGMs and (g) comparison of simulated field and NPL intensity distributions to experiment for the  $\text{TE}_{12,1}$  mode. The topography of each MD is shown in the leftmost inset in (a)–(c). Scan sizes for images and topography in (a), (b), and (c) are  $8 \times 8$ ,  $5 \times 5$ , and  $2.5 \times 2.5 \mu\text{m}^2$ , respectively. The center inset in (c) is the NPL intensity profile of the  $\text{TE}_{11,1}$  mode taken along a 5–11 o’clock line of the image. The NPL images in (d) and (e) are for  $\text{TE}_{35,1}$ ,  $\text{TE}_{32,2}$ , and  $\text{TE}_{24,3}$  ( $R=3 \mu\text{m}$ ) and  $\text{TM}_{21,1}$ ,  $\text{TE}_{24,1}$ , and  $\text{TE}_{21,2}$  ( $R=2 \mu\text{m}$ ), respectively. The images in (f) are  $1 \times 1 \mu\text{m}^2$  regions of  $\text{TM}_{22,1}$ ,  $\text{TE}_{25,1}$  ( $R=2 \mu\text{m}$ ),  $\text{TE}_{35,1}$  ( $R=3 \mu\text{m}$ ), and  $\text{TE}_{10,1}$  ( $R=1 \mu\text{m}$ ) mode images from (a)–(c) (see the small arrows marking the positions of these mode excerpts). In (g), images 1 and 2 are plots of  $I=E_x^2+E_y^2$  for multiple source excitation calculated at  $t=\tau_2$  and  $\tau_2/5$  ( $\tau_2=2 \text{ ps}$ ), respectively; image 3 is  $I=(E_x+E_0)^2+(E_y+E_0)^2$  of plot 2 (where  $E_0=|E_x^{\text{max}}|/2$ ); images 4 and 6 are “probe-diffused” plots of 1 and 3, respectively; and image 5 is the experiment.

Fig. 4(f)]. The smaller radial size observed for TM modes is in agreement with the FDTD calculations. We found that the number of azimuthal maxima observed experimentally is very close to the mode azimuthal number calculated by FDTD. This is also seen from Fig. 4(f) in which the linear separation between neighboring maxima is 450–600 nm, i.e., close to  $2\pi R/m$ .

## VI. DISCUSSION

Our observation of  $m$  maxima in the NPL images of the WGMs implies that we are observing the *field amplitude* distribution of the *emission intensity* or, in other words, a phase sensitivity of the NPL detection. One might naturally attribute this phase sensitivity to the contribution of FPMs and CMs, forming the background field in WGM images. Such a field contributes to the emission coming from the central region of the disk [see Figs. 2(a) and Fig. 3], and it is seen in the radial NPL profile presented in the inset of Fig. 4(c). The effect of the background field on the WGM and

NPL intensity distributions was simulated for the  $\text{TE}_{12,1}$  mode in Fig. 4(g) (images 1–4 and 6). Here, images 1 and 2 are the intensity of the total field  $I=E_x^2+E_y^2$  generated by five equivalent excitation sources placed near the edge (two), at the center (one) and at intermediate positions (two) at times  $\tau_2=2 \text{ ps}$  and  $\tau_2/5$ , respectively. Image 3 is the intensity distribution, which includes a contribution from the constant background field  $E_0=|E_x^{\text{max}}|/2$  added to field components from image 2, i.e., for  $t\sim\tau_2/5$ . Simulated “NPL” images 4 and 6 were obtained by a convolution of intensity images 1 and 3, respectively, with a two-dimensional Gaussian function having a spatial dispersion of 300 nm. At  $t\sim\tau_2$ , the intensity and NPL images [see images 1 and 4 in Fig. 4(g)] resolve only the WGM field, having  $2m$  equivalent azimuthal maxima. At  $t\sim\tau_2/5$ , the intensity images contain contributions of the FPMs and CMs, leading to a strong distortion of the WGM maxima (see image 2). In image 3, the interference between the WGM and  $E_0$  suppresses the negative field maxima. The resulting NPL image (6) shows a highly non-uniform WGM intensity distribution with the number of azimuthal maxima close to  $m$ , which is in good agreement with

the experiment (image 5). Thus, the observation in the experimental NPL images of *amplitude* structure ( $m$  maxima) instead of *intensity* structure ( $2m$  maxima) corresponds to field averaging during time  $t_2/5$  instead of field averaging during time  $\tau_2$ . This result indicates a shortening of the radiation process of the QD ensemble in the MD compared to macroscopic planar structures. This means that the assumptions of homogeneous radiation decay and the absence of mode reabsorption in the QD ensemble, which would lead to intensity imaging, are not valid. The inhomogeneous radiation decay of the QD ensemble in the MD can be expected in a weak-coupling regime due to the enhancement or suppression of the spontaneous emission rate<sup>6</sup> of differently located QDs (Purcell effect). Indeed, nearly a five times decrease in the radiative decay was observed for InAs QDs in resonance with a high- $Q$  mode ( $Q \sim 2 \times 10^3$ ) of a micropillar cavity.<sup>36</sup> We also cannot exclude the possibility of ultrafast reabsorption of the WGM through multiexcitonic states.<sup>37</sup> The discrimination between these two effects, namely, contributions of the Purcell effect and those of ultrafast reabsorption to the amplitude of the NPL imaging of WGMs in MDs, requires more detailed experiments, including the use of dilute QD ensembles and time-resolved measurements. Such experiments are in progress.

In Figs. 5(a) and 5(b), we compare the experimental and calculated  $m$  numbers versus wavelength for  $R=1, 2$ , and  $3 \mu\text{m}$ . One can see that, within the experimental and calculation uncertainties, the measured azimuthal numbers ( $m$  numbers) agree well with the calculations and that the experimentally determined  $m$  numbers correlate well with mode radial numbers ( $l$  numbers) and polarization (TE and TM). We found, however, a strong difference in the measured and calculated mode wavelengths for  $\text{TM}_{22,1}$  and  $\text{TM}_{23,1}$  [ $R=2 \mu\text{m}$ , Fig. 3(c)]. These differences, in our opinion, reflect the optical anisotropy of the AlGaAs waveguide consisting of an AlAs/GaAs superlattice and show the high sensitivity of the WGM mode positions to material properties.

## VII. CONCLUSIONS

In conclusion, we have used NPL spectroscopy with a spatial resolution below the light diffraction limit to study the optical fields of WGMs in GaAs and AlGaAs microdisks

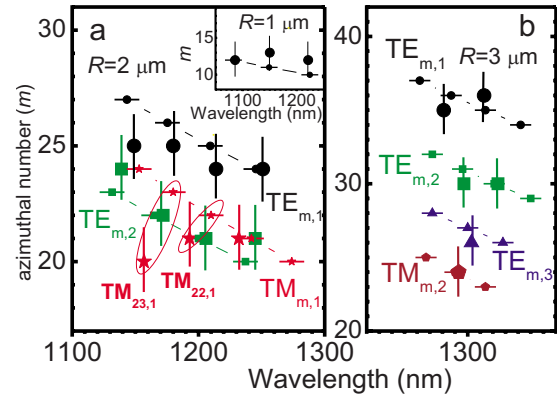


FIG. 5. (Color online) Calculated (small symbols) and measured (large symbols) spectral dependence of azimuthal numbers for  $\text{TE}_{m,1}$  (circles),  $\text{TE}_{m,2}$  (squares),  $\text{TE}_{m,3}$  (triangles),  $\text{TM}_{m,1}$  (stars), and  $\text{TM}_{m,2}$  (pentagons) for MDs having  $R$  ( $\mu\text{m}$ ): (a) 2 and (b) 3 and 1—inset in (a). The horizontal and vertical bars show the calculation and experimental uncertainties, respectively.

(radii  $R=1-3 \mu\text{m}$  and quality factors  $Q \sim 5 \times 10^3$ ) containing InAs quantum dots (QDs) emitting in the range of  $1.1-1.3 \mu\text{m}$ . WGMs having azimuthal numbers  $m=10-36$  and radial numbers  $l=1-3$  together with low- $Q$  FPMs and CMs have been observed in the NPL spectra. A dispersion of the WGM positions of  $0.2 \text{ nm}$  and an enhancement of the TM-mode intensities were observed in spatially resolved NPL spectra. We found that spectrally resolved NPL intensity images of WGMs reveal  $m$  azimuthal maxima around the disk circumference, which corresponds to the period of the field amplitude. Using FDTD calculations, we show that the amplitude imaging arises from the interference between the WGMs and a background field formed by FPMs and CMs, and that such interference reflects strong spatial inhomogeneity of the radiation decay in the QD ensemble. We demonstrate a direct measurement of WGM quantum numbers by using NPL imaging, which shows good agreement with the FDTD calculations.

## ACKNOWLEDGMENTS

The authors wish to acknowledge the NATO Science for Peace Program (Grant No. SfP.982735) and the Notre Dame Equipment Restoration Program for support of this research.

<sup>1</sup>Lord Rayleigh, *Scientific Papers* (Cambridge University, Cambridge, UK, 1912), Vol. 5, p. 617.

<sup>2</sup>S. L. McCall, A. F. J. Levi, R. E. Slusher, S. J. Pearton, and R. A. Logan, *Appl. Phys. Lett.* **60**, 289 (1992).

<sup>3</sup>M. Borselli, T. Johnson, and O. Painter, *Opt. Express* **131**, 515 (2005).

<sup>4</sup>B. Gayral, J. M. Gerard, A. Lemaitre, C. Dupuis, L. Manin, and J. L. Pelouard, *Appl. Phys. Lett.* **75**, 1908 (1999).

<sup>5</sup>K. Srinivasan, M. Borselli, T. J. Johnson, P. E. Barclay, and O. Painter, *Appl. Phys. Lett.* **86**, 151106 (2005).

<sup>6</sup>L. C. Andreani, G. Panzarini, and J. M. Gerard, *Phys. Rev. B* **60**, 13276 (1999).

<sup>7</sup>E. Peter, P. Senellart, D. Martrou, A. Lemaitre, J. Hours, J. M. Gerard, and J. Bloch, *Phys. Rev. Lett.* **95**, 067401 (2005).

<sup>8</sup>J. Renner, L. Worschech, A. Forchel, S. Mahapatra, and K. Brunner, *Appl. Phys. Lett.* **89**, 091105 (2006).

<sup>9</sup>Zhaoyu Zhang, Lan Yang, Victor Liu, Ting Hong, Kerry Vahala, and Axel Scherer, *Appl. Phys. Lett.* **90**, 111119 (2007).

<sup>10</sup>J. S. Xia, K. Nemoto, Y. Ikegami, Y. Shiraki, and N. Usami, *Appl. Phys. Lett.* **91**, 011104 (2007).

- <sup>11</sup>N. Louvion, D. Gerard, J. Mouette, F. de Fornel, C. Seassal, X. Letartre, A. Rahmani, and S. Callard, *Phys. Rev. Lett.* **94**, 113907 (2005).
- <sup>12</sup>A. M. Mintairov, Y. Tang, J. L. Merz, V. Tokranov, and S. Oktyabrsky, *Phys. Status Solidi C* **2**, 845 (2005).
- <sup>13</sup>J. C. Knight, N. Dubreuil, V. Sandoghdar, J. Hare, V. Lefevre-Saguin, J. M. Raimond, and S. Haroche, *Opt. Lett.* **21**, 698 (1996).
- <sup>14</sup>E. Moreau, I. Robert, J. M. Gerard, I. Abram, L. Manin, and V. Thierry-Mieg, *Appl. Phys. Lett.* **79**, 2865 (2001).
- <sup>15</sup>A. Imamoglu, D. D. Awschalom, G. Burkard, D. P. DiVincenzo, D. Loss, M. Sherwin, and A. Small, *Phys. Rev. Lett.* **83**, 4204 (1999).
- <sup>16</sup>K. Hennessy, A. Bodalato, M. Wigner, D. Gerace, M. Atature, S. Gulde, S. Falt, E. L. Hu, and A. Imamoglu, *Nature (London)* **445**, 896 (2007).
- <sup>17</sup>A. M. Mintairov, K. Sun, J. L. Merz, C. Li, A. S. Vlasov, D. A. Vinokurov, O. V. Kovalenkov, V. Tokranov, and S. Oktyabrsky, *Phys. Rev. B* **69**, 155306 (2004).
- <sup>18</sup>X. Zhu, Y. Zhang, Y. Xin, G. Wang, R. Wang, Y. Ling, H. Zhou, Y. Yin, B. Zhang, L. Dai, G. Zhang, and Z. Gan, *J. Microsc.* **194**, 439 (1999).
- <sup>19</sup>D. J. Shin, H. Y. Ryu, S. H. Kim, H. G. Park, and Y. H. Lee, in *Lasers and Electro-Optics Society, 2001, The 14th Annual Meeting of the IEEE*, Vol. 2, p. 661.
- <sup>20</sup>R. Quidant, J.-C. Weeber, A. Dereux, G. Leveque, J. Weiner, and C. Girard, *Phys. Rev. B* **69**, 081402(R) (2004).
- <sup>21</sup>N. N. Ledentsov, V. M. Ustinov, V. A. Schukin, P. C. Kop'ev, Z. I. Alferov, and D. Bimberg, *Semiconductors* **32**, 343 (1998).
- <sup>22</sup>S. Blokhin, N. Kryzhanovskaya, A. Gladyshev, N. Maleev, A. Kuz'menkov, E. Tanklevskaya, A. Zhukov, A. Vasil'ev, E. Semenova, M. Maximov, N. Ledentsov, V. Ustinov, E. Stock, and D. Bimberg, *Semiconductors* **40**, 476 (2006).
- <sup>23</sup>V. Tokranov, M. Yakimov, A. Katsnelson, M. Lamberti, and S. Oktyabrsky, *Appl. Phys. Lett.* **83**, 833 (2003).
- <sup>24</sup>A. M. Mintairov, T. H. Kosel, J. L. Merz, P. A. Blagnov, A. S. Vlasov, V. M. Ustinov, and R. E. Cook, *Phys. Rev. Lett.* **87**, 277401 (2001).
- <sup>25</sup>A. M. Mintairov, P. A. Blagnov, J. L. Merz, V. M. Ustinov, A. S. Vlasov, A. R. Kovsh, J. S. Wang, L. Wei, and J. Y. Chi, *Physica E (Amsterdam)* **21**, 385 (2004).
- <sup>26</sup>I. Smotrova and A. I. Nosich, *Opt. Quantum Electron.* **36**, 213 (2004).
- <sup>27</sup>A. Yariv, N. S. Kapany, and J. J. Burke, *Optical Waveguides, Quantum Electronics — Principles and Applications* (Academic, New York, 1972).
- <sup>28</sup>G. Panzarini and L. C. Andreani, *Phys. Rev. B* **60**, 16799 (1999).
- <sup>29</sup>M. Gurioli, A. Vinattieri, M. Zamfirescu, M. Colocci, S. Sanguinetti, and Richard Nötzel, *Phys. Rev. B* **73**, 085302 (2006).
- <sup>30</sup>M. De Giorgi, C. Lingk, G. von Plessen, J. Feldmann, S. De Rinaldis, A. Passaseo, M. De Vittorio, R. Cingolani, and M. Lomascolo, *Appl. Phys. Lett.* **79**, 3968 (2001).
- <sup>31</sup>K. Matsuda, T. Saiki, H. Saito, and K. Nishi, *Appl. Phys. Lett.* **76**, 73 (2000).
- <sup>32</sup>M. Bayer and A. Forchel, *Phys. Rev. B* **65**, 041308 (2002).
- <sup>33</sup>B.-J. Li and P.-L. Liu, *IEEE J. Quantum Electron.* **32**, 1583 (1996).
- <sup>34</sup>S. C. Hagness, D. Rafizadeh, S. T. Ho, and A. Taflove, *J. Light-wave Technol.* **15**, 2154 (1997).
- <sup>35</sup>Y. Xu, R. K. Lee, and A. Yariv, *Phys. Rev. A* **61**, 033808 (2000).
- <sup>36</sup>J. M. Gerard, B. Sermage, B. Gayral, B. Legrand, E. Costard, and V. Thierry-Mieg, *Phys. Rev. Lett.* **81**, 1110 (1998).
- <sup>37</sup>E. Dekel, D. Regelman, D. Gershoni, E. Ehrenfreund, W. V. Schoenfeld, and P. M. Petroff, *Phys. Rev. B* **62**, 11038 (2000).